# Effect of the surface morphology of 3D printed titanium substrates on the mode I fracture toughness of metal-metal and metal-composite bonded joints

Gulino, Michele; de Araujo Alves Lima, Rosemere; Moroni, Fabrizio; Pirondi, Alessandro; Teixeira De Freitas, S.

**DOI**
10.1016/j.tafmec.2024.104778

**Publication date**
2025

**Document Version**
Final published version

**Published in**
Theoretical and Applied Fracture Mechanics

Theoretical and Applied Fracture Mechanics 135 (2025) 104778

Contents lists available at ScienceDirect

Theoretical and Applied Fracture Mechanics

journal homepage: www.elsevier.com/locate/tafmec

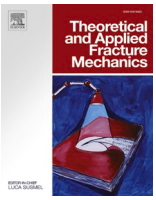

# Effect of the surface morphology of 3D printed titanium substrates on the mode I fracture toughness of metal-metal and metal-composite bonded joints

Michele Gulino [a,*], Rosemere de Araujo Alves Lima [b], Fabrizio Moroni [a], Alessandro Pirondi [a], Sofia Teixeira de Freitas [b,c]

[a] Department of Engineering for Industrial Systems and Technologies, University of Parma, Parma, Italy
[b] Faculty of Aerospace Engineering, Delft University of Technology, Delft, the Netherlands
[c] IDMEC, Instituto Superior Técnico, Universidade de Lisboa, Lisboa, Portugal

ARTICLE INFO

*Keywords:*
Fracture toughness
Titanium Ti6Al4V
Carbon fibre reinforced polymer (CFRP)
Laser powder bed fusion (LPBF)
Co-bonding

ABSTRACT

Parts manufactured with Laser Powder Bed Fusion (LPBF) are drawing interest in the adhesive joints research because of their high surface roughness, which is usually associated with good adhesion. This work aims to assess the adhesion strength of the inherent surface morphology of LPBF manufactured titanium.

Double Cantilever Beam (DCB) tests were carried out to determine the mode I fracture toughness of joints comprising as-printed titanium (Ti6Al4V) adherends, namely titanium-titanium secondary bonded and titanium-Carbon Fibre Reinforced Polymer (CFRP) co-bonded joints. The effect of high-temperature oxidation on the fracture toughness was also evaluated by testing a batch of joints in which the titanium underwent a post-printing thermal treatment. The as-printed specimens were compared to the same type of joints but with sandblasted titanium adherends to evaluate the effect of this surface pre-treatment on the value of fracture toughness.

The results indicate that non-oxidised titanium joints with untreated adherends had an average of 11% higher fracture toughness than their sandblasted counterparts. On the other hand, sandblasting proved beneficial for oxidised joints, increasing the fracture toughness by 64% on average over the untreated samples.

## 1. Introduction

Technologically intensive industrial sectors, such as aerospace and automotive, are striving to reduce the weight of their products, as they are pushed by stringent regulations on environmental impact and the need for low operational costs to address the necessities of final consumers.

Weight reduction calls for the use of composite materials, such as Fibre Reinforced Polymers (FRPs), which have higher strength and stiffness-to-weight ratios compared to metals.

In large structures such as aircraft, FRP laminates are often joined with other materials (e.g. aluminium or titanium) to improve their crashworthy capabilities [1,2] and thermal resistance [3]. For instance, the Airbus A350, a relatively newly designed aircraft, is made of 53 % FRPs, followed by aluminium (19 %) and titanium (14 %) alloys [4].

In this context, adhesive bonding is a well-suited technique to join FRPs and metals. Compared to mechanical fastening, it provides a wider load-bearing area and eliminates the need to drill the composite adherends, reducing stress concentrations and potential delaminations [5]. Furthermore, it saves weight, especially in long bond lines requiring several rivets or bolts [6,7].

Despite its many advantages over other joining techniques, adhesive bonding still needs to overcome significant technical challenges. Proper adhesion usually requires surface treatments to promote good wettability of the substrates, remove contaminants (e.g. release agents) and promote interlocking [8–10]. However, such treatments are time-consuming and hardly performed with good repeatability, potentially leaving spots with weak adhesion. Since such defects are not detectable by Non-Destructive Inspection (NDI) techniques and can lead to sudden failure, adhesive joints are yet to be certified in aircraft's primary structures, where they are often superseded by hybrid adhesive-riveted joints [11,12].

* Corresponding author.
*E-mail address:* michele.gulino@unipr.it (M. Gulino).

https://doi.org/10.1016/j.tafmec.2024.104778
Received 6 August 2024; Received in revised form 28 October 2024; Accepted 24 November 2024
Available online 26 November 2024

Another challenge is posed by the low inter-laminar fracture toughness of thermoset composite laminates, which in the case of secondary-bonded or co-bonded joints is most of the time lower than the adhesive, triggering crack deflection in the FRP plies [13–15].

To address this issue, in the context of metal-composite joining, many researchers have been focusing on the manufacturing of pin-shaped protrusions in the metal adherend penetrating the through-the-thickness direction of the laminate to arrest delamination, [16–24], in a similar fashion to Z-pins in composites [25].

It is worth mentioning that Additive Manufacturing (AM), and notably Laser Powder Bed Fusion (LPBF), represents a strategic technology to produce structured interfaces, having potentially no limits in the choice of geometry and increasingly reliable with the introduction of in-situ monitoring methods to avoid manufacturing defects and to reduce inter-build variations [26–28].

Particularly, AM, in the form of Direct Metal Laser Sintering, was used by Parkes et al. [23] to build an array of pins on a titanium substrate, which was then co-cured with a CFRP laminate to form a Single Lap Joint (SLJ) coupon. The results proved that the ultimate tensile strength, elongation at break and absorbed energy were significantly higher than those of the baseline specimens without pins.

LPBF was employed by Raimondi et al. [24], where pyramidal lattice structures were printed onto a steel substrate to then be infiltrated by an Advanced Sheet Moulding Compound (ASMC) composite via compression moulding to manufacture pull-out test samples. The presence of the lattices significantly improved pull-out load and absorbed energy, with the only drawback being that these types of printed structures can only be infiltrated by short-fibre composites.

Moreover, LPBF printed parts have a peculiar surface morphology with high roughness [29–32], which is often associated with good adhesion strength [6]. Therefore, using LPBF as-built substrates in metal–metal or metal-composite adhesive joints could be a promising alternative for the time- and cost-demanding surface treatments, if not even to manufacture complex pin-like structures.

The adhesion strength of the as-printed LPBF surface in metal–metal bonded joints has been studied in three different works by Ertürk [33], Koch [34], and Ardila-Rodríguez [35], where joints with untreated LPBF printed adherends have been compared to similar joints but with treated adherends. The results showed that the as-printed LPBF surface offered a comparable [35] or even higher [33] adhesion strength than the one of the surface-treated joints.

Nevertheless, the literature on assessing the adhesion of as-built LPBF substrates bonded with composite laminates is limited. To the authors' knowledge, only two works on the topic can be found [36,37].

In the investigation of Nguyen [36], LPBF titanium was either co-cured with CFRP or bonded with another LPBF titanium adherend, without undergoing surface treatment, to form DCB joints. The results showed that the inherent LPBF surface morphology promoted mechanical interlocking between the resin and the partially melted particles on the LPBF titanium substrate, leading to mostly cohesive failure and crack deflection in the composite.

In the work of Fielden-Stewart et al. [37], it was shown that the mixed-mode fracture toughness of LPBF aluminium-CFRP secondary bonded joints printed with several build angles was higher for untreated joints compared to mechanically abraded joints, regardless of the build angle.

Moreover, titanium LPBF parts commonly undergo a post-printing thermal treatment to relieve residual stresses. To the authors' knowledge, the adhesion strength of thermally oxidised and non-thermally oxidised LPBF components has only been compared with Ti6Al4V-dental porcelain joints [38]. The results indicated that forming an increasingly thick oxide scale with the temperature prevented good adhesion due to the oxide detaching from the base metal.

It should be noted that there is a gap in the literature regarding the comparison of the mode I fracture toughness of treated (meaning both thermally treated after the printing process and surface treated before bonding) and as-printed metal–metal and metal-composite bonded joints involving LPBF adherends. In particular, a comparison between metal-composite co-bonded joints with treated and untreated LPBF printed adherends is currently lacking in the literature.

To cover this gap, in this work, DCB joints are tested with as-printed LPBF Ti6Al4V adherends and compared with sandblasted LPBF Ti6Al4V, in a similar way to a previous work by the authors of this paper involving joints with LPBF −printed AlSi10Mg [39]. In addition, the influence of high-temperature oxidation is evaluated via the testing of DCB joints where the titanium adherend undergoes a post-printing thermal treatment to relieve residual stresses. While thermal treatment is a common procedure for LPBF parts, investigating its influence on the fracture toughness of bonded joints is also lacking in the literature.

Therefore, the aim and the novelty of this work are twofold: 1) to assess the adhesion of LPBF parts without surface treatment, and 2) to understand the influence of thermal oxidation on the adhesion strength of LPBF parts.

## 2. Materials, methods and dissimilar DCB design

### 2.1. Titanium adherends

The LPBF Ti6Al4V adherends (130x25x6 $mm^3$) were supplied by 3T-Additive Manufacturing Ltd (Newbury, United Kingdom), and were printed in an M290 LPBF machine (EOS Gmbh, Krailling, Germany). The Ti6Al4V powder had an average particle diameter of 37.3 μm, and the adherends were printed with a 90° build angle (Fig. 1), 60 μm layer thickness, 1250 mm/s laser scan speed, 190 W laser power and 80 μm spot size. A total of 36 adherends were manufactured, 24 for metal–metal joints and 12 for metal-composite joints. The adherends were printed with an integrated loading block and drilled to allow the load application on the testing machine.

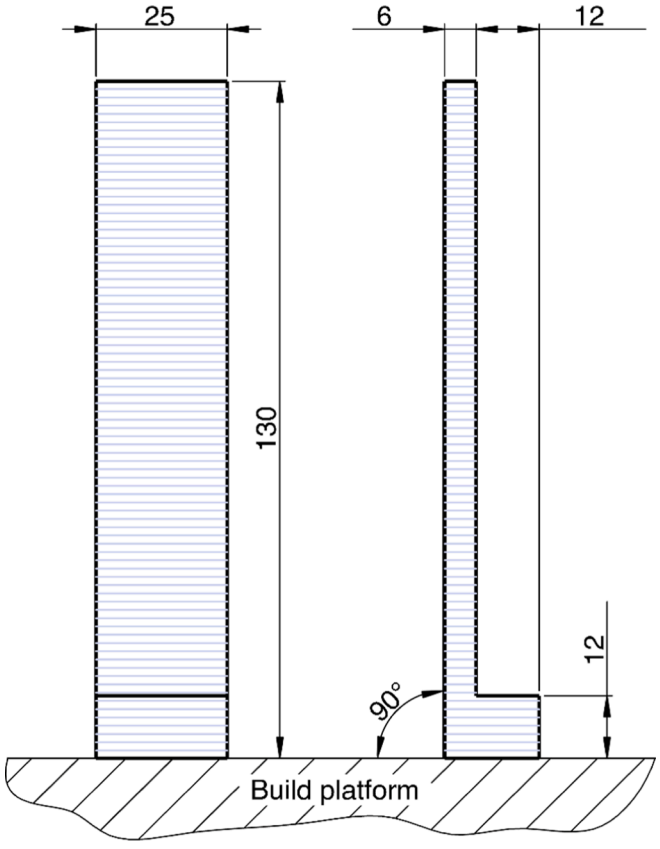


**Fig. 1.** Titanium adherends, front view on the left and side view on the right. Grey horizontal lines represent the layers. All dimensions are in millimetres.

**Table 1**
(d) stands for datasheet and (e) for experimentally evaluated. $E_{ti}$ is the young's modulus of titanium, CPT is the Cured Ply Thickness, $E^{t}_{cfrp}$ is the longitudinal modulus of the composite ply (warp direction), $E_{cfrp\ and}$ $G_{cfrp}$ are the flexural and out-of-plane shear moduli of the laminate ($[0–90]_{13}$) stacking sequence.

| $E_{ti}$ (e) | $G_{ti}$ [41] | $E^{t}_{cfrp}$ (d) | $E_{cfrp}$ (e) | $G_{cfrp}$ (e) | CPT (d) |
|---|---|---|---|---|---|
| **MPa** | **MPa** | **MPa** | **MPa** | **MPa** | **mm** |
| 118,030 | 44,041 | 62,680 | 60,079 | 2556 | 0.624 |

Half of the titanium adherends underwent a post-printing thermal treatment at 800 °C for 4 h in a vacuum furnace ($1.3x10^{-3}$ mBar maximum air pressure) to relieve the residual stresses due to the rapid heating and cooling cycles of the LPBF process. In this work, the thermally oxidised adherends will be referred to as "oxidised".

To retrieve Young's modulus of the Ti6Al4V adherends, 4 dogbone tensile test coupons according to the ASTM E8 standard [40], with a 6x2 $mm^2$ cross-sectional area and 25 mm gauge length were printed using the same parameters of the substrates. The tests were carried out on an MTS servo-hydraulic machine with a 25 kN load cell, 10 mm/min displacement rate and an external extensometer to monitor the strains on the coupons, as detailed in a previous work by the authors of this paper [39]. The resulting Young's modulus is 118030 MPa.

### 2.2. CFRP adherends

For the manufacturing of the co-bonded Ti6Al4V-CFRP joints, woven GG630T (T700 carbon fibres) – DT120 prepregs were provided by Bercella Srl (Varano de' Melegari, Italy), with an estimated cured ply thickness (CPT) of 0.624 mm and a longitudinal modulus in the direction of the warp, $E^{t}_{cfrp}$ of 62680 MPa (from the company's datasheet). The stacking sequence of the CFRP adherend was $[0–90]_{13}$, with the number of plies (13) set to achieve pure mode I in the composite-to-metal bonded joints, as described in the next section of the paper.

To assess the bending ($E_{cfrp}$) and out-of-plane shear ($G_{cfrp}$) moduli of the CFRP laminate, needed for the data reduction method, 3-point bending (3pb) tests were carried out following the same procedure as in the previous investigation by the authors of this paper [39]. The displacement in the mid-section of the 3pb samples was retrieved with the 3D Digital Image Correlation (DIC) technique and compared to the displacement evaluated with the analytical model of a Timoshenko beam:

$$\delta = \frac{F/2\left(L/2\right)^{3}}{3E_{cfrp}I} + 1.2\frac{F/2\,L/2}{G_{cfrp}A} \tag{1}$$

Where F is the test load,L is the span length, I and *A* are the moment of inertia and the area of the rectangular cross-section of the 3pb specimens, respectively.

The experimental displacement was calculated for 5 different span lengths and then fitted with the analytical formula, choosing the best-fit values for the bending and out-of-plane shear modulus [39], which are shown in Table 1, together with the CPT, the CFRP longitudinal modulus, and the Young's and shear moduli of the titanium adherends. The latter was calculated using a Poisson's coefficient of 0.34 [41].

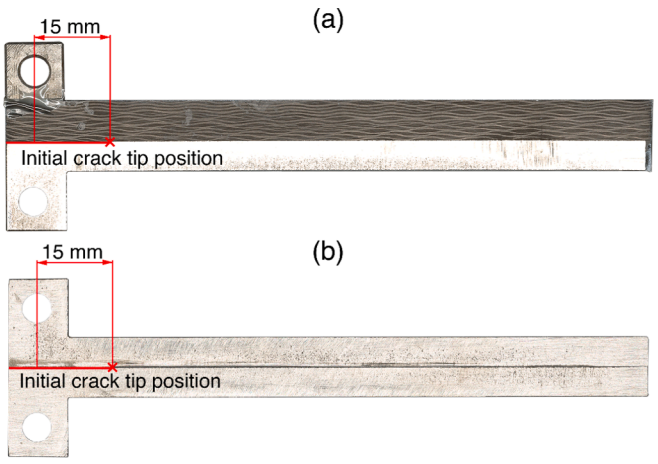


**Fig. 2.** (a) Co-bonded joints with loading block glued to the CFRP adherend. (b) Titanium-titanium joints. All the joints have an initial crack length of 15 mm from the load application point.

### 2.3. Design of DCB dissimilar joints

To achieve pure mode I loading at the crack tip of the dissimilar titanium-CFRP DCB, the longitudinal strain-based criterion was used [42]. In this criterion, the arms of the DCB specimens are designed such that:

$$E_{ti}h_{ti}^{2} = E^{f}_{cfrp}h_{cfrp}^{2} \tag{2}$$

$h_{cfrp}$ and $h_{ti}$ are the thicknesses of the CFRP and titanium adherends, respectively. $E_{ti}$ is the Young's modulus of the titanium adherend, and $E^{f}_{cfrp}$ is the longitudinal bending stiffness of the composite substrate. The latter can be calculated according to the Classic Laminate Theory (CLT) as:

$$E^{f}_{cfrp} = 12/D^{*}11hcfrp3 \tag{3}$$

With D11*being the element in the first row and first column of the inverse bending stiffness matrix of the laminate. Considering a stacking sequence of $[0–90]_{n,}$ where n is the number of plies yet to be determined, $D^{*}_{11}$ is equal to 3.59E-7 $Nmm^{-1}$ regardless of the number of plies, thus $E^{f}_{cfrp}$ is equal to 62680 MPa (Eq. (3)). According to Eq. (2), knowing the thickness of the titanium adherends of 6 mm and its Young's modulus of 118030 MPa, the resulting target thickness to achieve pure mode I is 8.23 mm. Considering the estimated CPT of 0.624 mm (Table 1), the final target thickness of the laminate was rounded down to 8.11 mm using 13 plies.

### 2.4. Test matrix and DCB joints manufacturing

A total of 24 joints were manufactured, namely 12 titanium-titanium secondary bonded joints and 12 titanium-CFRP co-bonded joints. For each of these categories of joints, half of the titanium adherends were oxidised, while the remaining half did not go through any post-printing thermal treatment. Finally, regarding the surface pre-treatment, half of the titanium adherends were sandblasted for each subtype of joints prior

**Table 2**
Naming of the samples.

| | **Oxidised Ti6Al4V substrates** | | **Non-Oxidised Ti6Al4V substrates** | |
|---|---|---|---|---|
| | **As-printed** | **Sandblasted** | **As-printed** | **Sandblasted** |
| **Ti6Al4V-Ti6Al4V secondary-bonded** | TT-O AP | TT-O S | TT-NO AP | TT-NO S |
| **Ti6Al4V-CFRP co-bonded** | TC-O AP | TC-O S | TC-NO AP | TC-NO S |

**Table 3**
Dimensions of the DCB samples. The thickness of the adhesive $h_{adh\_TC}$ for the TC joints is assumed to be equal to that of the carrier mat.

| | $b$ | $h_{tot\_TT}$ | $h_{ti}$ | $h_{adh\_TT}$ | |
|---|---|---|---|---|---|
| | mm | mm | mm | mm | |
| **TT-O AP** | 24.91 ± 0.02 | 12.24 ± 0.03 | 6.07 ± 0.02 | 0.11 ± 0.01 | |
| **TT-O S** | 24.88 ± 0.02 | 12.22 ± 0.02 | 6.02 ± 0.01 | 0.18 ± 0.01 | |
| **TT-NO AP** | 24.82 ± 0.05 | 12.29 ± 0.01 | 6.11 ± 0.01 | 0.07 ± 0.02 | |
| **TT-NO S** | 24.82 ± 0.03 | 12.26 ± 0.01 | 6.06 ± 0.03 | 0.13 ± 0.00 | |
| | $b$ | $h_{tot\_TC}$ | $h_{ti}$ | $h_{cfrp}$ | $h_{adh\_TC}$ |
| | mm | mm | mm | mm | mm |
| **TC-O AP** | 24.82 ± 0.07 | 14.44 ± 0.07 | 6.04 ± 0.06 | 8.29 ± 0.02 | 0.10 |
| **TC-O S** | 24.88 ± 0.04 | 14.46 ± 0.01 | 6.09 ± 0.05 | 8.27 ± 0.05 | 0.10 |
| **TC-NO AP** | 24.78 ± 0.02 | 13.90 ± 0.01 | 6.00 ± 0.08 | 7.80 ± 0.07 | 0.10 |
| **TC-NO S** | 24.80 ± 0.01 | 13.82 ± 0.05 | 6.01 ± 0.03 | 7.71 ± 0.07 | 0.10 |

to bonding, and the remaining half had no abrasion surface treatment. The test matrix and the corresponding names of the samples are shown in Table 2.

The sandblasting was performed with alumina particles at 0.5 MPa air pressure, with a nozzle-to-surface distance approximately equal to 10 cm to evenly cover the entire surface in approximately 20 s.

All titanium adherends were cleaned in an ultrasonic acetone bath for 10 min before bonding to remove dirt and contaminants from the surface.

The joints were bonded with Hexbond ST 1035 (Hexcel, Stamford, USA) supported epoxy adhesive film, with a polyester carrier mat of 300 g/m$^2$ areal density, nominal lap shear strength of 41 MPa and curing temperatures ranging from 90 °C to 150 °C [43]. A carrier mat thickness of 0.10 mm was measured with a digital micrometre screw gauge after dissolving the epoxy matrix of the film in acetone.

The metal-composite co-bonded joints were manufactured by Bercella Srl (Varano de' Melegari, Italy) via autoclave and vacuum bag, with a curing cycle of 130 °C for 2 h at 6 bar of pressure. The 13 prepreg plies were stacked on a metal plate treated with a release agent, followed by the adhesive film and the titanium adherends. A Teflon strip was placed at the tip of the joints to create an artificial crack positioned 15 mm ahead of the load application axis.

After curing, the co-bonded joints were machined to match the width and length of the titanium adherends, and a loading block (Fig. 2) was bonded to the CFRP adherend with Loctite EA 3425 bicomponent paste epoxy (Henkel AG&CO. KGaA, Düsseldorf, Germany).

The metal–metal joints were bonded in an autoclave with a vacuum bag using a mould with pins to avoid relative motion between the adherends. As for the metal composite joints, a Teflon strip was used to create the initial defect at 15 mm ahead of the load application axis. The curing cycle was the same as used for metal-composite co-bonded joints. (Fig. 2).

The bondline thickness of the titanium-CFRP joints was not controlled by any system, as per practice in industrial co-bonding processes. The same choice was adopted for the titanium-titanium joints, to have a more significant comparison with the TC joints.

The final dimensions of the joints are listed in Table 3. The width $b$, the total thickness of the TT joints $h_{tot\_TT}$, and the thickness of the titanium adherends $h_{ti,}$ were measured with a digital calliper. The thickness of the adhesive for the titanium-titanium joints ($h_{adh\_TT}$) was calculated as the difference between the total thickness and the sum of the adherends thickness. Digital pictures of the specimens' sides were taken using a Keyence VR-5000 wide-area 3D non-contact measurement system (Fig. 2), to evaluate the thickness of the CFRP adherends $h_{cfrp}$. Unfortunately, the adhesive layer in the titanium-CFRP joints was not clearly visible from the side pictures. $h_{cfrp}$ was therefore evaluated by subtracting the thickness of the carrier mat and the titanium adherend to the total thickness of the joint, thus assuming that the adhesive thickness of the titanium-CFRP joints $h_{adh\_TC}$ is equal to the one of the carrier mat.

It can be seen from Table 3 that the co-bonded joints with oxidised titanium adherends TC-O have a thickness almost matching the target for pure mode I (8.28 mm on average), while the TC-NO joints are thinner (7.76 mm on average). The influence of the CFRP adherends' thickness on the percentage of mode II will be discussed in section 3 *Mode mixity calculation of dissimilar DCB*.

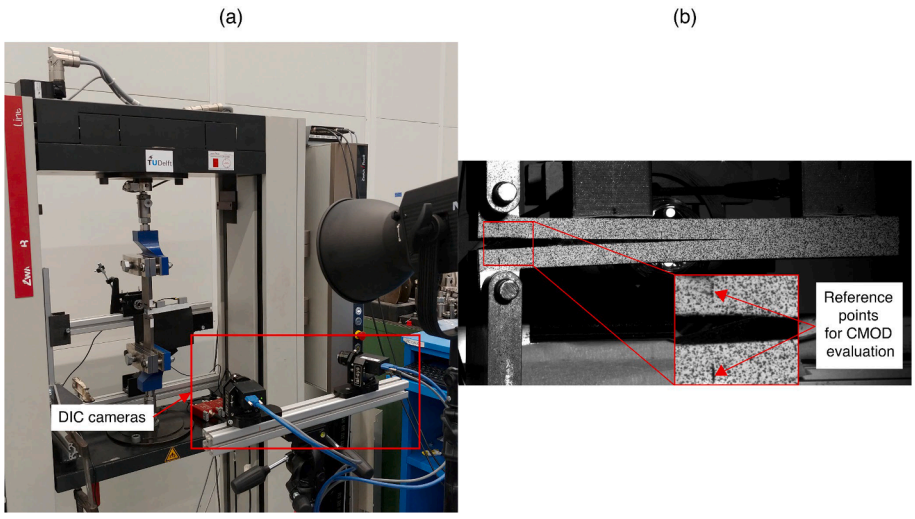


**Fig. 3.** (a) Test setup with 3D DIC cameras. (b) The speckle pattern on the sample is used to evaluate the Crack Mouth Opening Displacement (CMOD) with a virtual extensometer using Digital Image Correlation (DIC), with the ROI highlighted in red.

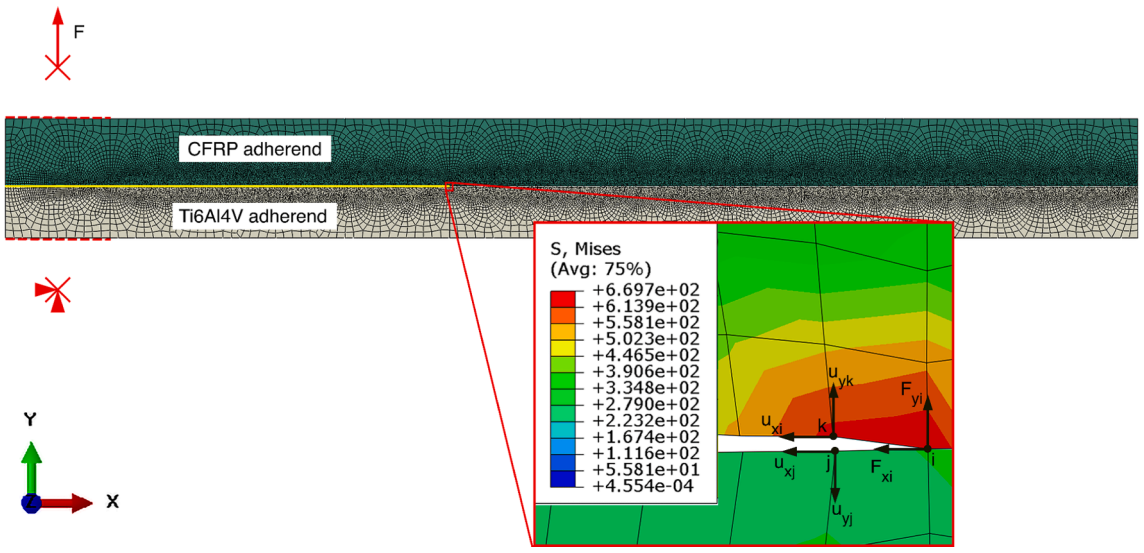


**Fig. 4.** Plane strain DCB model, with VCCT fracture criterion implemented in the contact interaction between the CFRP and the Ti6Al4V adherends. The crack is modelled as the unbonded node region in the contact (yellow line). The load and the boundary conditions are applied via two reference points rigidly connected to the nodes indicated with the dashed red lines in the figure, representing the loading blocks.

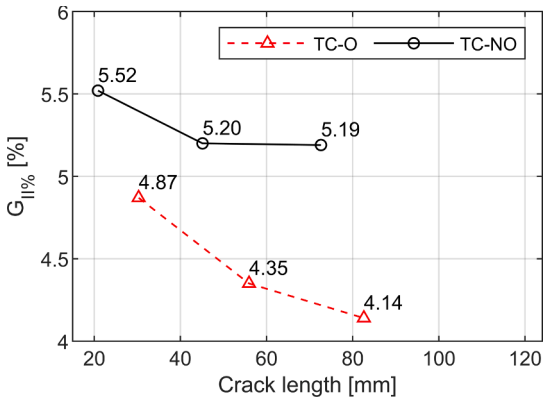


**Fig. 5.** The Mixed mode I/II percentage of TC-O and TC-NO joints was calculated for three crack lengths.

### 2.5. Test setup

A speckle pattern was painted on the side edges of the DCB samples to monitor the Crack Mouth Opening Displacement (CMOD) with a virtual extensometer via 3D DIC, using the Vic3D software by Correlated Solutions Inc. DIC cameras with 5 Megapixels sensors and 23 mm of focal length were positioned at 57.4 cm from the samples, and the pictures were taken with a 2 Hz frequency. The Region Of Interest (ROI) was defined around the load application (Fig. 3), and it was discretised using a 33 pixels subset and an 11 pixels step size.

The joints were tested according to the ASTM D3433 standard [44] under displacement control at 2.5 mm/min with a Zwick-Roell electric testing machine equipped with a 10 kN load cell (Fig. 3). The testing machine was synchronised with the DIC acquisitions, and the tests ended when the crosshead displacement reached 6 mm.

The Compliance Beam Based Method (CBBM) [45,46] was chosen to perform the data reduction of the DCB tests. The method works for both symmetric and asymmetric joints, and it allows for the evaluation of the crack tip position knowing the compliance of the DCB during the test, avoiding the visual assessment of the crack length, which is often not trivial due to crack branching and crack deflection to different composite plies.

In this work, the compliance of the joints was evaluated as the linear regression of the CMOD-load curve, sampled during 14 unloading phases. The unloadings occurred every 0.4 mm of crosshead displacement, returning to 75 % of the total displacement with a 10 mm/min unloading rate. For instance, the 10th unloading occurred at 4 mm, returning to 3 mm.

### 2.6. Data reduction method

According to the CBBM model, which is based on the Timoshenko beam theory, the compliance of the DCB joint is calculated as follows:

$$C^s = \left(\frac{CMOD}{F}\right)_s = \frac{8a^3}{E_{ti}bh_{ti}^3} + \frac{12a}{5bh_{ti}G_{ti}} \tag{4}$$

For symmetric joints ($C^s$), and

$$C^{as} = \left(\frac{CMOD}{F}\right)_a = \frac{a^3}{3}\left(\frac{1}{E_{ti}I_{ti}} + \frac{1}{E_{cfrp}I_{cfrp}}\right) + \frac{6a}{5b}\left(\frac{1}{h_{ti}G_{ti}} + \frac{1}{h_{cfrp}G_{cfrp}}\right) \tag{5}$$

For asymmetric joints ($C^{as}$), where $F$ is the load measured during the test, $b$ is the width of the DCB specimens, and $I_{ti}$, $I_{cfrp}$ are the second-order moment of the cross-sectional area for the titanium and CFRP, respectively.

Knowing the evolution of the compliance during the test, it is possible to retrieve the crack length from Eq. (4) and Eq. (5). Thus, the mode I fracture toughness for symmetric joints, $G_{Ic}^s$, can be evaluated as

$$G_{Ic}^s = \frac{6F^2}{b^2h_{ti}}\left(\frac{2a^2}{h_{ti}^2E_{ti}} + \frac{1}{5G_{ti}}\right) \tag{6}$$

For asymmetric joints, $G_{Ic}^{as}$ is

$$G_{Ic}^{as} = \frac{F^2}{2b}\left[a^2\left(\frac{1}{E_{ti}I_{ti}} + \frac{1}{E_{cfrp}I_{cfrp}}\right) + \frac{6a}{5bG_{cfrp}}\left(\frac{1}{h_{ti}} + \frac{1}{h_{cfrp}}\right)\right] \tag{7}$$

It must be noted that since the Fracture Process Zone (FPZ) ahead of the crack tip influences the joint's compliance, the crack length $a$ inherently takes into account the length of the FPZ [45,46].

No correction for large deflections was applied to the crack length evaluation since the maximum CMOD at the end of the test was around 5.5 mm for most of the samples, with a corresponding crack propagation up to 124 mm (the whole bonding surface) for some samples. Large

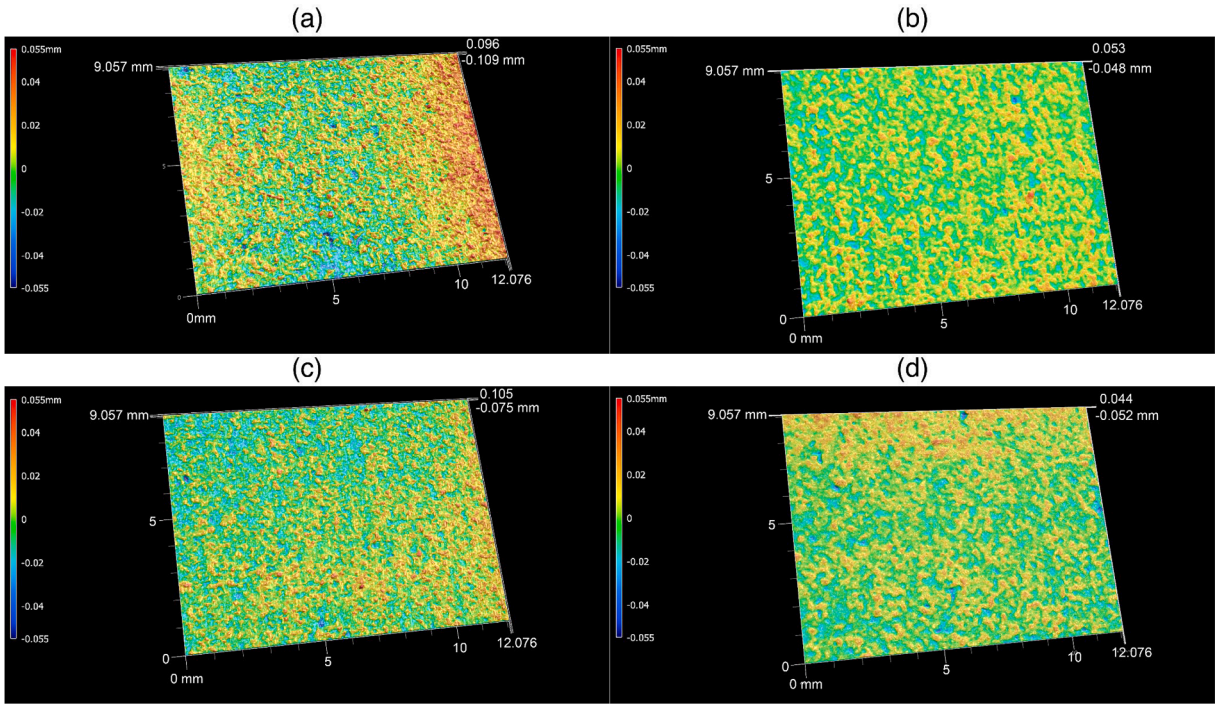


**Fig. 6.** Optical profilometries of the 4 types of surfaces: (a) oxidised as-printed, (b) oxidised sandblasted, (c) non-oxidised as-printed and (d) non-oxidised sandblasted. The coloured scale represents the surface height in the specimen's surface.

**Table 4**
Average and standard deviation on 3 scans per sample of surface parameters for (a) oxidised as-printed, (b) oxidised sandblasted, (c) non-oxidised as-printed and (d) non-oxidised sandblasted.

| | **Oxidised** | | **Non-oxidised** | |
|---|---|---|---|---|
| | **As-printed** | **Sandblasted** | **As-printed** | **Sandblasted** |
| **Sa [µm]** | 10.95 ± 1.72 | 7.53 ± 0.21 | 9.26 ± 0.18 | 7.13 ± 0.32 |
| **Sz [µm]** | 198.8 ± 5.13 | 110.56 ± 20.65 | 156.66 ± 18.98 | 105.79 ± 13.26 |
| **Ssk [-]** | 0.37 ± 0.02 | 0.13 ± 0.06 | 0.23 ± 0.08 | −0.10 ± 0.13 |
| **Sku [-]** | 3.98 ± 0.36 | 3.69 ± 0.51 | 3.63 ± 0.18 | 3.71 ± 0.43 |

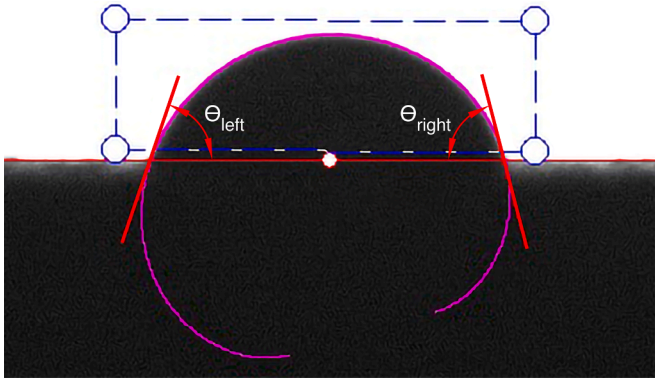


**Fig. 7.** Distilled water droplet with indication of left and right angles. Curve fitting in purple.

deflections are considered relevant by the standard ISO 15024 [47] when the ratio between the CMOD and the crack length is bigger than 0.4 ($CMOD/a > 0.4$). In this specific work, this condition is never met due to the relatively high bending stiffness of the substrates.

Finally, it is worth underlining that the $G_{Ic}$ herein evaluated is the apparent value, that is specific to the fracture process zone and failure mechanism (cohesive, interfacial or delamination, see section 4 *Results and discussion*) developed in these joints.

### *2.7. Optical profilometry, contact angle measurements, and x-ray diffraction (XRD) analysis*

The bonding surface of 4 spare titanium adherends, one for each surface type (oxidised as-printed, oxidised sandblasted, non-oxidised as-printed and non-oxidised sandblasted), was characterised in terms of morphology, wettability and chemical composition.

Optical profilometry was carried out on a Keyence VR-5000 wide-area 3D non-contact measurement system, scanning 3 areas (9x12 $mm^2$) along the central portion of the bondline of each sample to evaluate the surface arithmetic mean height $S_a$, maximum peak height $S_z$, skewness $S_{sk}$ and kurtosis $S_{ku}$.

Contact angle measurements were performed with a KSV Instruments CAM 200 optical angle meter using a 10 µl drop of distilled water. For each sample, 3 drops were analysed within 30 s from their release on the surface.

**Table 5**
Distilled water contact angles.

| | **Oxidised** | | **Non-oxidised** | |
|---|---|---|---|---|
| | **As-printed** | **Sandblasted** | **As-printed** | **Sandblasted** |
| **θ [°]** | 91.27 ± 4.04 | 58.94 ± 6.73 | 89.44 ± 3.86 | 77.00 ± 2.95 |

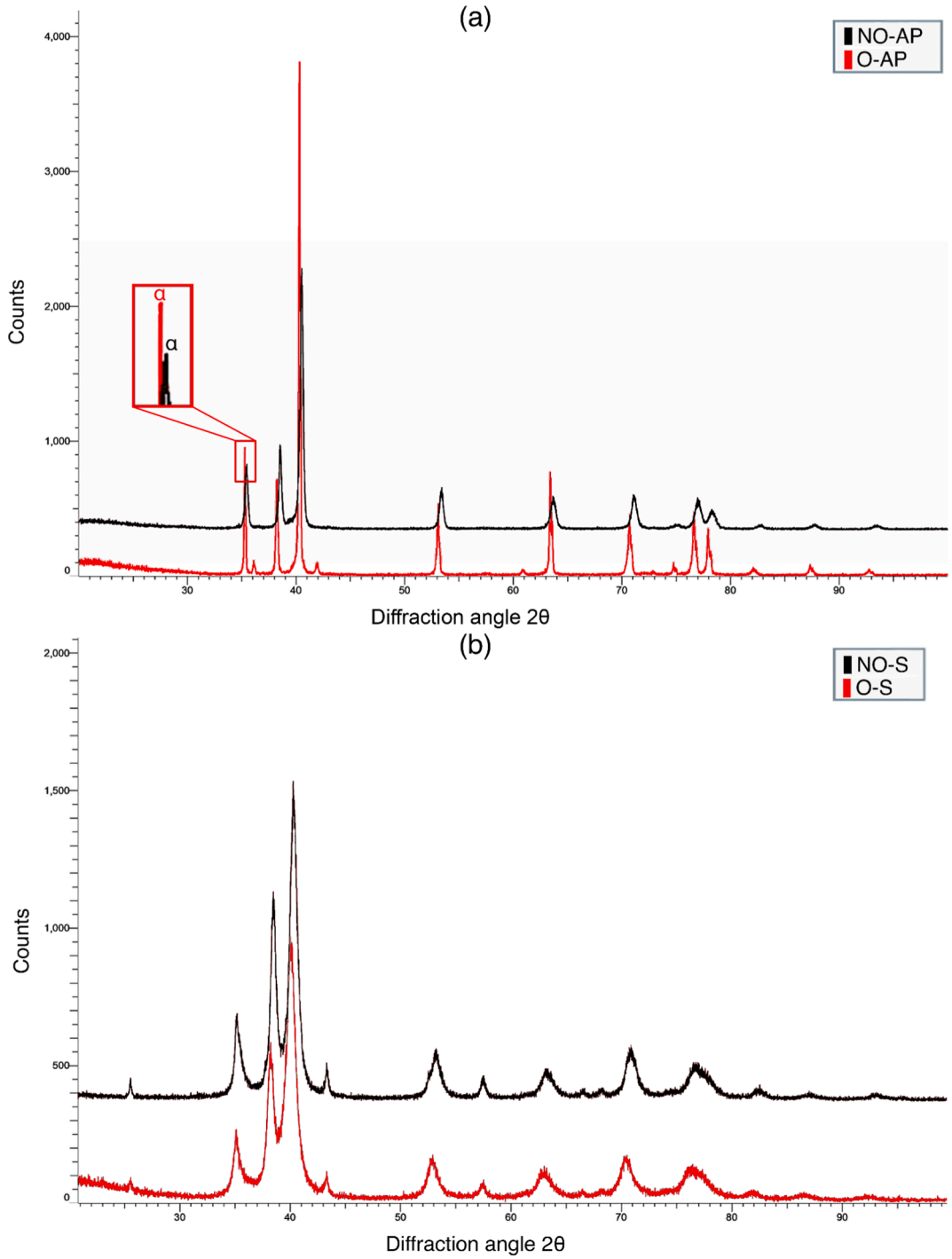


**Fig. 8.** XRD spectra for (a) as-printed samples with a magnification on the titanium- α shift to the left and (b) sandblasted samples. The red lines indicate the oxidised samples, which are represented below the non-oxidised samples (i.e. at lower counts).

In addition, X-Ray Diffraction (XRD) was performed using a Bruker D8 Advanced diffractometer with Cu-Kα source and Lynxeye-XE-T position sensitive detector, scanning the range of 20° to 100° diffraction angles $2\theta$.

## 3. Mode mixity calculation of dissimilar DCB

To calculate the pure mode II component of the DCB joints, the loading mixed-mode ratios, defined as the mode II component divided by the total strain energy release rate, were determined with Virtual Crack Closure Technique (VCCT) in the Finite Element Modelling (FEM) software Abaqus, according to the method described in the work by Wang et al. [42].

Two-dimensional DCB models were developed, meshing the substrates with quadrilateral plane strain linear elements with reduced integration (CPE4R), as shown in Fig. 4. The element size in the vicinity of the bonded area was set to 0.05 mm after a mesh convergence study. The titanium adherend was modelled as elastic isotropic with Young's modulus of 118030 MPa (Table 1), assuming a Poisson ratio of 0.34 [41]. The CFRP adherend was modelled as elastic orthotropic, using the experimental values of out-of-plane shear and flexural modulus from Table 1. Not having any available experimental data, the modulus in the

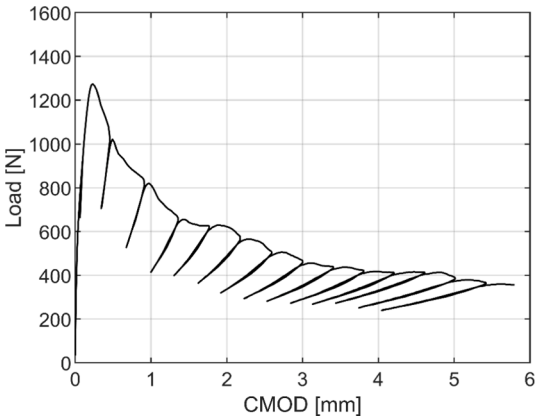


**Fig. 9.** Load-CMOD curve for TT-NO AP1 DCB joint.

Y direction (see the triad in Fig. 4) and the out-of-plane Poisson ratio were assumed to be 10000 MPa and 0.3, respectively.

A VCCT fracture criterion was implemented in the contact definition between the two arms of the DCB. According to the VCCT, the mode I and mode II energy release rates are defined as

$$G_I = \left[F_{yi}\left(u_{yk} - u_{yj}\right)\right]/2aB \tag{8}$$

$$G_{II} = \left[F_{xi}\left(u_{xk} - u_{xj}\right)\right]/2aB \tag{9}$$

Where $\Delta a$ is the increment of crack length (which is equal to the element size of 0.05 mm), $b$ is the joint's width (Table 3), while $F$ and $u$ are the contact forces and nodal displacements at the node $i$, which is the shared node at the crack tip, and the adjacent nodes $j$ and $k$ (Fig. 4).

For both the TC-O and the TC-NO DCB models, three initial crack lengths were analysed: the length at the first unloading, at the 5th unloading and the 10th unloading. For each crack length, the corresponding mode I load from the experimental test was applied. The loads and the boundary conditions are applied via two reference points rigidly connected to the DCB arms at the nodes corresponding to the position of the loading blocks (Fig. 4).

The critical strain energy release rate was set to 10 kJ/m$^2$, deliberately high enough to avoid crack propagation with the applied loads.

Therefore, the mode II percentage for the TC-O and TC-NO joints can be evaluated from Eq. (8) and Eq. (9) for each crack length as

$$GII\% = 100G_{II}/(G_I + G_{II}) \tag{10}$$

The mode II percentage for the TC-O and TC-NO joints is plotted against the three crack lengths in Fig. 5. The VCCT results show that the mode II percentage remains fairly constant during the crack propagation, with average values of 4.5 % for the TC-O joints and 5.3 % for the TC-NO joints. Given the low mode II percentage and the negligible difference between the TC-O and TC-NO batches, the results presented in the next sections of the paper should be close to the pure mode I condition even for the metal-composite joints. For this reason, the mode II percentage

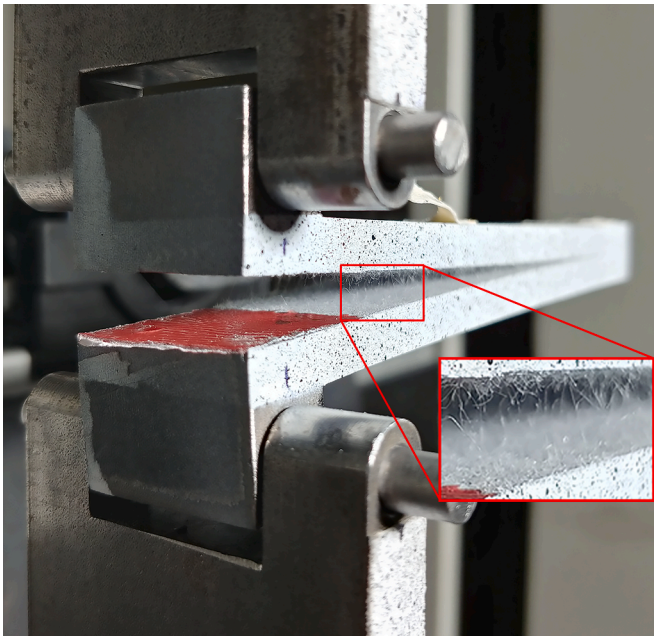

**Fig. 11.** Bridging of the polyester carrier mat.

**Table 6**
Steady-state fracture toughness and maximum load during test for each batch of samples.

| | TT-O AP | TT-O S | TT-NO AP | TT-NO S |
|---|---|---|---|---|
| **Steady-state $G_{Ic}$ [kJ/m$^2$]** | 0.47 ± 0.17 | 0.79 ± 0.13 | 0.87 ± 0.12 | 0.53 ± 0.17 |
| **$F_{max}$ [N]** | 713.35 ± 202.00 | 954.09 ± 144.23 | 1300.05 ± 68.08 | 1270.06 ± 60.25 |

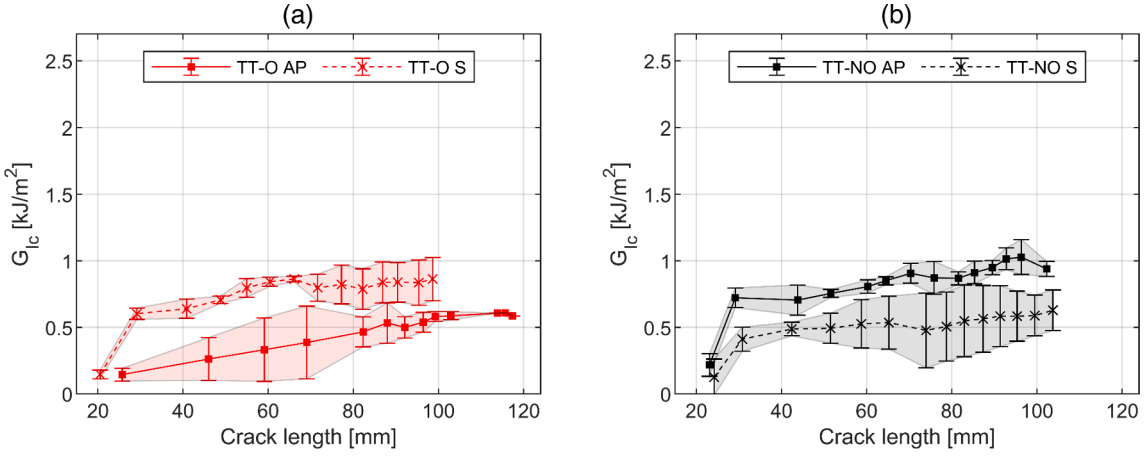


**Fig. 10.** R-curves for the titanium-titanium joints. The average fracture toughness is plotted against the average crack length for each unloading, and the standard deviation is also reported with vertical bands. For the TT-O AP batch, the test ended prematurely (before completing all the 14 unloading) for all 3 samples with catastrophic failure and complete separation of the adherends.

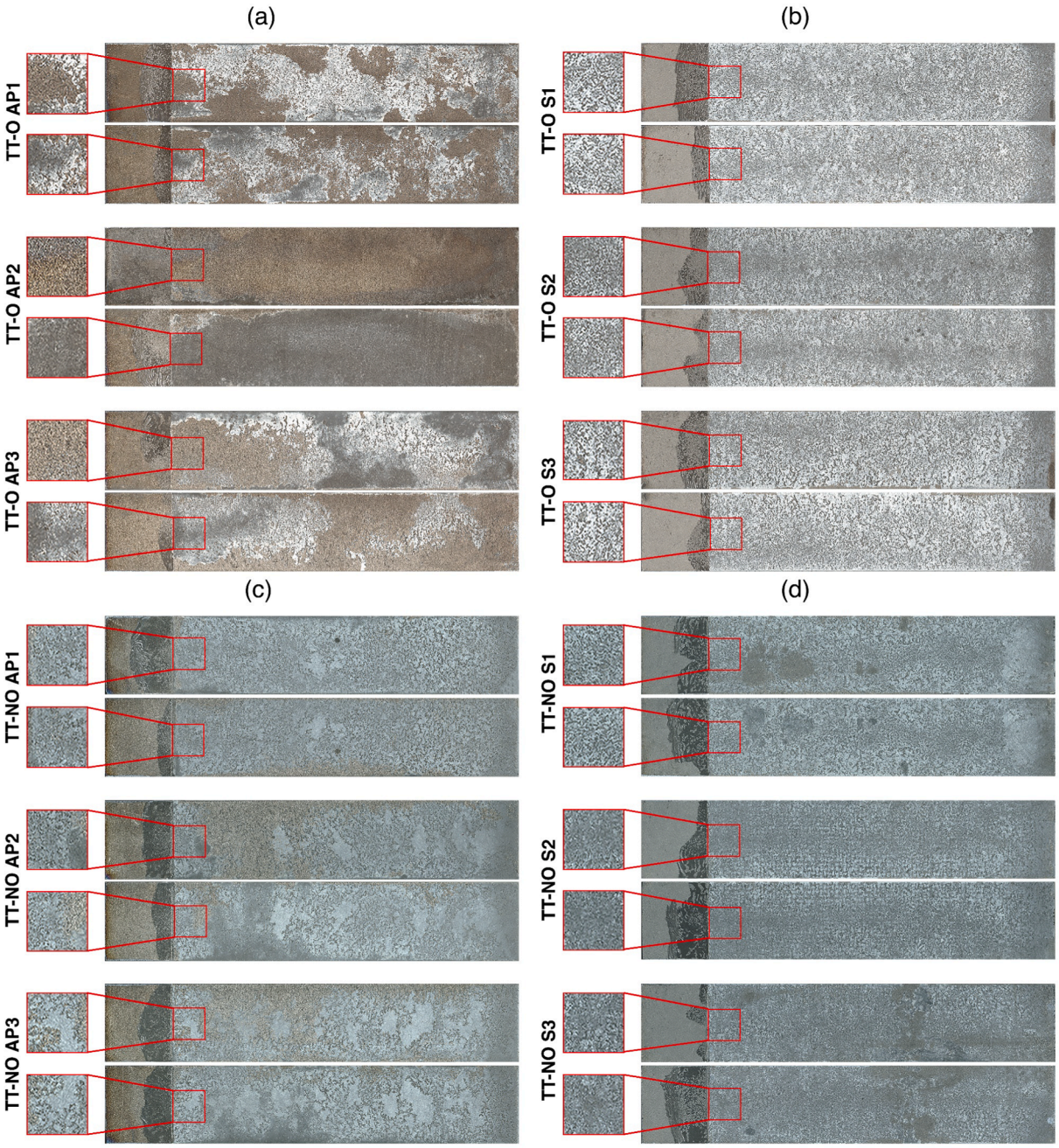


**Fig. 12.** Fracture surfaces of titanium-titanium joints. The crack initiation area has been highlighted and enlarged.

will be neglected when referring to the TC joints in the next sections of the paper.

## 4. Results and discussion

### 4.1. Titanium surface characterisation

#### 4.1.1. Surface roughness evaluation

The optical profilometries and the deriving surface parameters are shown in Fig. 6 and Table 4, respectively.

The three-dimensional optical reconstructions show a notable difference between the as-printed and sandblasted surfaces, with the latter having an overall smoother texture as confirmed by the lower arithmetical mean height $S_a$ and maximum height $S_z$. The sandblasting treatment, though, did not influence the shape of the surface asperities, which are overall quite sharp, as shown by $S_{ku}$ values greater than 3.

The $S_{sk}$ values are generally close to 0, showing how, for each surface type, the waviness is almost normally distributed around the mid-plane. Nevertheless, it is worth noting how the as-printed surfaces have higher $S_{sk}$ values, suggesting the presence of high peaks skewed above the mid-plane, possibly related to the presence of partially melted powder particles stuck on the surface.

It is also worth noting that the as-printed oxidised surface has a higher (+12 %) roughness compared to the non-oxidised one. While the difference is below the standard deviation of the $S_a$ of the AP-O samples, this higher roughness could be likely due to the oxidation occurring during the thermal treatment, as found in [38] for samples treated above 750 °C.

#### 4.1.2. Wettability evaluation

The distilled water contact angles have been calculated by curve fitting the contour of the liquid droplets' pictures. The angle formed

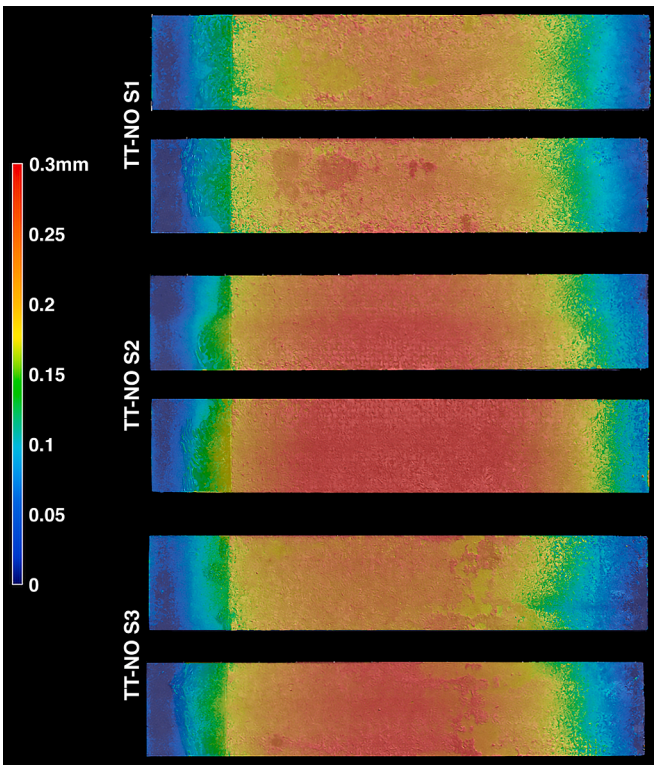


**Fig. 13.** Height profiles of the TT-NO S joints taken with a Keyence VR-5000 wide area optical profilometer. The central portion of the adherends is higher than the extremities.

between the curve tangents at the right and left sides of the droplets and the titanium surface were averaged to obtain the contact angle Θ (Fig. 7).

Table 5 shows how the sandblasting treatment substantially improves the surface's wettability, consistently reducing the value by about 25 %.

According to the findings of Ardila-Rodríguez et al. [35], it is possible that, given the high roughness of the LPBF printed substrates, the acetone cleaning is not sufficient to remove all the contaminants in the deep valleys of the as-printed samples surface, resulting in higher contact angle measurements. On the other hand, the lower contact angle of the sandblasted surfaces suggests that an acetone bath sufficiently cleans this type of sample.

Moreover, it has already been observed in the literature that roughness has a significant effect on the wettability of a surface [48,49]. According to the Cassie-Baxter model [49], air pockets between the solid and the liquid phase prevent the drop to properly wet the surface, and an increase in roughness leads to an increase in number of air pockets. For instance, in the work by Thenard et al. [50] etching on the surface of LPBF Ti6Al4V samples reduced the roughness and the skewness of their surface but at the same time increased its wettability, as found in the results of this work.

#### *4.1.3. XRD spectroscopy analysis*

The scope of XRD was to assess the presence of oxides on the surface of the titanium substrates, which were thermally treated in a vacuum furnace.

The XRD spectra of the 4 types of surfaces are shown in Fig. 8. Some considerations can be made regarding the spectra of the as-printed samples.

First, it must be noted that the peaks of titanium-α (around 35°, 38° and 41° diffraction angles) of the O-AP spectrum are slightly shifted to the left compared to the ones in the non-oxidised baseline (NO-AP). This behaviour was also observed in [51], where conventionally manufactured Ti6Al4V was annealed for 4 h at 700 °C in a water vapour atmosphere and compared to untreated reference specimens.

Furthermore, as in [51,52], alumina ($Al_2O_3$) peaks with a total weight percentage of 0.8 % were found only in the O-AP spectrum at around 26°, 35°, 38°, 43°, 53°, 58°, 67°,68°, 72°, 81°, 84°, 86°, 89°, 91° and 95°, being a further indicator of thermal oxidation, given the presence of aluminium in a range of 5.5 to 6.75 wt% in the Ti6Al4V powder composition (from datasheet).

The peaks found at 36° and 41.5° in the oxidised spectrum are indexed as Rutile ($TiO_2$) according to the ICSD database, suggesting thermal oxidation such as in [51–53]. It is worth mentioning that vanadium carbide (VC) was found on the surface of the oxidised specimens

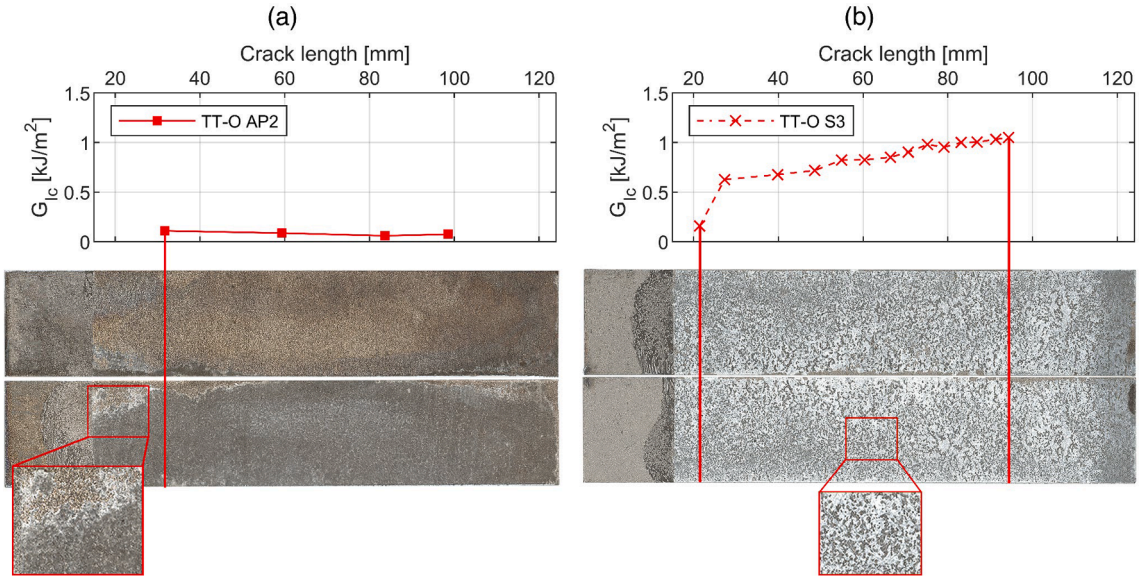


**Fig. 14.** (a) Sample TT-O AP2. purple line indicating the start of the test. failure in the oxide layer leading to low fracture toughness, which was evaluated only on 4 points due to the test ending prematurely. (b) Sample TT-O S3, green lines representing the beginning and end of the test. small voids attributable to cavitation occurring during the curing cycle. according to the cbbm method, the crack tip position considers the FPZ, thus the crack length at the first unloading is shifted forward compared to the position of the teflon strip.

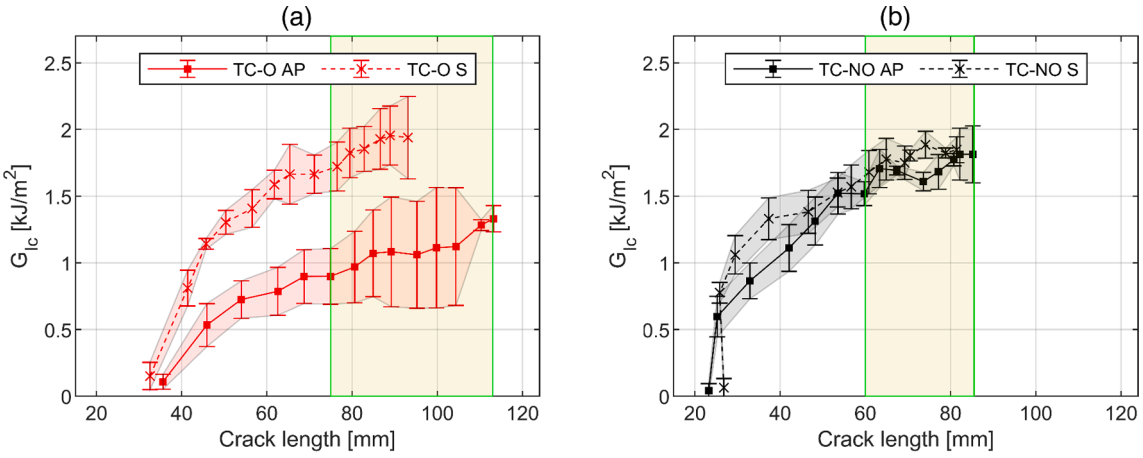


**Fig. 15.** R-curves of the titanium-CFRP samples. As for the titanium-titanium joints, 3 sample per batch were tested, and the plot shows the average fracture toughness against the average crack length for each unloading. The shaded region is bound by the standard deviation of the fracture toughness for each unloading. The region of steady-state crack propagation is highlighted in green.

**Table 7**
Initial fracture toughness, average fracture toughness, steady-state fracture toughness and maximum load for titanium-CFRP joints. The first unloading was discarded for the initial and average fracture toughness evaluation.

| | TC-O AP | TC-O S | TC-NO AP | TC-NO S |
|---|---|---|---|---|
| **Initial $G_{Ic}$ [kJ/m$^2$]** | 0.53 ± 0.16 | 0.81 ± 0.13 | 0.60 ± 0.15 | 0.78 ± 0.08 |
| **Average $G_{Ic}$ [kJ/m$^2$]** | 0.99 ± 0.32 | 1.60 ± 0.37 | 1.46 ± 0.39 | 1.56 ± 0.34 |
| **Steady-state $G_{Ic}$ [kJ/m$^2$]** | 1.04 ± 0.15 | 1.82 ± 0.06 | 1.72 ± 0.05 | 1.82 ± 0.05 |
| **$F_{max}$ [N]** | 863.57 ± 236.80 | 1140.50 ± 190.37 | 1316.80 ± 81.09 | 1535.60 ± 68.67 |

with a 1.5 % weight percentage, with peaks at 61°, 73°, 77° and 91° diffraction angles. The presence of VC on the samples' surface is unclear to the authors and would need further investigation.

Conversely, no major difference was found in the O-S and NO-S spectra for the sandblasted samples. This means that the abrasion of the surface has removed the traces of oxidation treatment performed prior. It is also interesting to note that a significant weight percentage of alumina was found on the surface of both samples (around 9 %), almost certainly related to sand particles stuck in the adherends during the sandblasting.

### 4.2. *Fracture behaviour of titanium − titanium joints*

#### 4.2.1. *Fracture toughness and R-curves of TT joints*

The load-CMOD curve for sample TT-NO AP1 is shown in Fig. 9 as an example. The R-curves for the TT-O and TT-NO joints are shown in Fig. 10. For each unloading, the average fracture toughness of each batch of samples is plotted against the average crack length.

For all the 4 groups, a minor increase of the R-curve during the crack propagation can be observed, likely due to the bridging of the fibres in the carrier mat of the film adhesive (Fig. 11). Nevertheless, since the trend of the curves is almost constant, a steady-state value of fracture toughness is calculated as the average of $G_{Ic}$ over all the unloadings excluding the first, which for most of the samples occurred before the crack started to propagate (i.e. $G_I < G_{Ic}$). The values of fracture toughness for the titanium-titanium joints are reported in Table 6, together with the maximum load reached during the test.

For the TT-O batch (Fig. 10**a**), the sandblasting treatment significantly increased the fracture toughness and maximum load. In contrast, the TT-NO joints (Fig. 10**b**) displayed an opposite trend, with the as-printed samples resulting in higher toughness than the sandblasted ones.

#### 4.2.2. *Analysis of the fracture surfaces and failure modes of TT joints*

The behaviour of the R-curves can be explained by looking at the fracture surfaces of the TT-O and TT-NO joints shown in Fig. 12, Fig. 13 and Fig. 14.

For the TT-O AP batch (Fig. 12**a**), the TT-O AP1 and T-O AP3 specimens displayed a mixed cohesive-adhesive failure, while the TT-O AP2 specimen failed in the oxide layer of the upper adherend as shown in Fig. 14**a**, where dark debris of oxides covering the adhesive can be seen on the bottom adherend, while only a few traces of the adhesive can be found on the top adherend. Thus, the overall lower performance of the TT-O AP joints is likely due to the presence of the brittle layer of oxide, which broke under much lower loads compared to the adhesive-oxide interface (adhesive failure) and in the adhesive itself (cohesive failure).

On the other hand, the sandblasting effectively removed the oxide layer originating from high temperature-oxidation during the thermal treatment, leading to cohesive failure for all the samples in the TT-O S batch (Fig. 12**b**), with higher fracture toughness compared to the TT-O AP batch (+68 %, Table 6). Indeed, as shown for sample TT-O S3 in Fig. 14**b**, the failure was cohesive with presence of adhesive on both substrates and an R-curve rising effect likely due to carrier mat fibre bridging.

The TT-NO joints showed an opposite behaviour compared to the TT-O batch, with the TT-NO S specimens having a 39 % lower fracture toughness than the TT-NO AP samples (Table 6). This behaviour can be explained by looking at the height profiles of the fracture surfaces of the TT-NO S samples (Fig. 13), where it can be seen that the central portion of the substrates (contoured in red) is higher than the extremities (contoured in blue), indicating that most likely the adherends are bent.

The bending of the adherends can be explained by the fact that the TT-NO batch did not undergo the thermal post-printing treatment, thus having non-negligible residual stresses then released during the sandblasting treatment. With the high-pressure curing cycle, the steel mould forced the substrates to deform elastically into a straight configuration, pre-tensioning the adhesive before the test, possibly leading to a lower fracture toughness value.

It is interesting to note that voids inside the adhesive layer are present in all the titanium-titanium joints, as can be seen in Fig. 12 and in better detail in Fig. 14**b**. The voids are likely attributable to gas

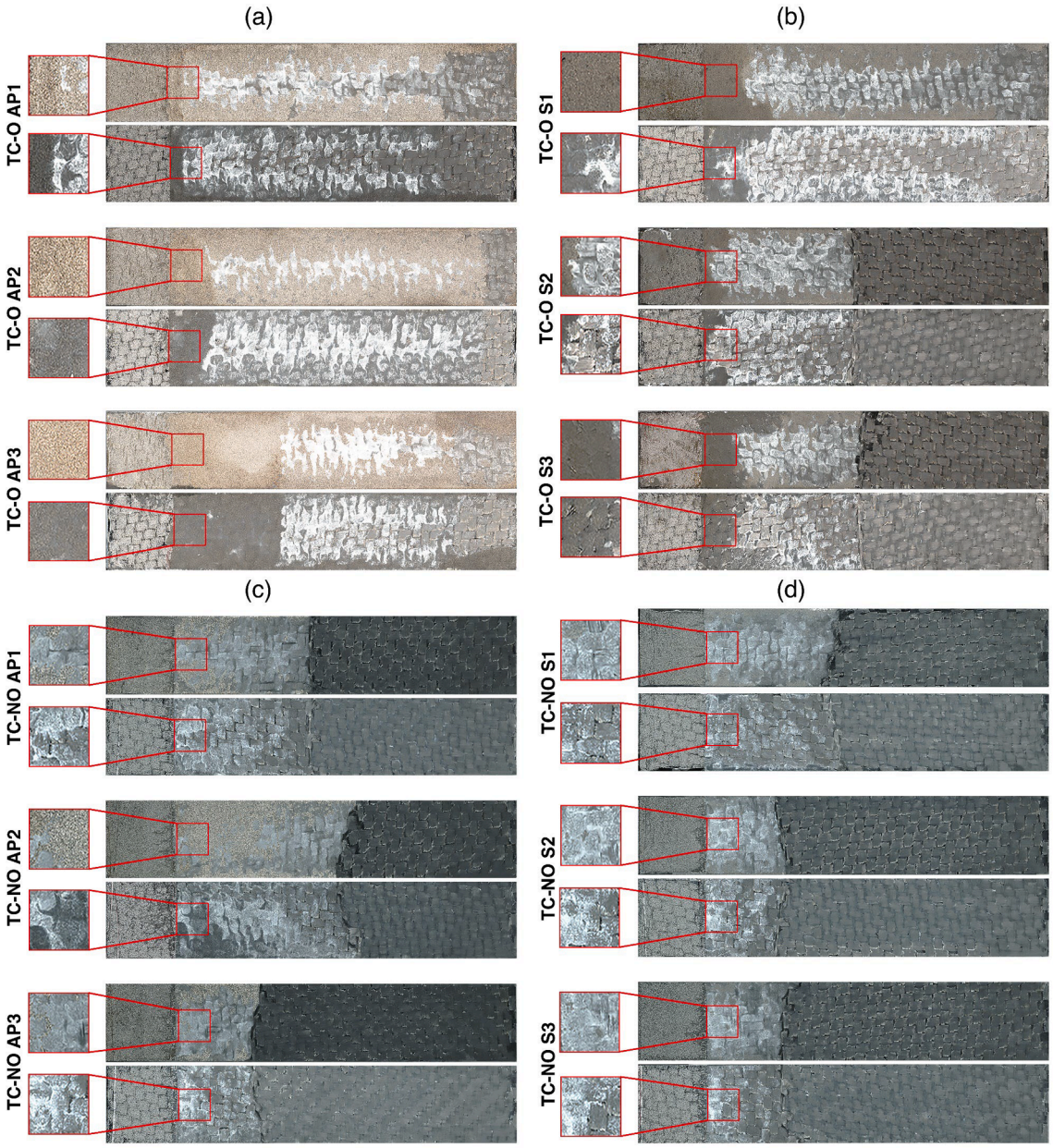


**Fig. 16.** Fracture surfaces of the titanium-CFRP samples, with enlargement of the crack the initiation area. For each joint, the titanium adherend is displayed below the CFRP adherend.

developed during the curing cycle, entrapped between the substrates without any way to escape through the steel mould. Consequently, while the TT-S O joints exhibited cohesive failure without bending of the adherends, the fracture toughness was impaired by the presence of these voids. Indeed, the steady state mode I fracture toughness of the adhesive (without voids) has been calculated in a previous work by the authors of this paper, resulting in 1.18 kJ/m$^2$ for aluminium-aluminium DCB joints with cohesive failure [39].

### 4.3. Fracture behaviour of titanium – CFRP joints

#### 4.3.1. Fracture toughness and R-curves of TC joints

The R-curves for the titanium-CFRP joints are shown in Fig. 15. A remarkable rising R-curve effect characterises the tests, which partially stabilized in the last part of the crack propagation, approximately from 75 mm onward for the TC-O batch and from 60 mm onward for the TC-NO batch. These crack length values were used for the evaluation of a steady state fracture toughness as the average value of the linear regression of the fracture toughness for each batch. Table 7 shows the initial, average, steady state fracture toughness and maximum load.

It is evident that the sandblasting significantly increased the toughness of the oxidised specimens while having a less significant effect on non-oxidised joints. In this case, the bending of the non-oxidised sandblasted samples due to the release of residual stresses had a minor influence on the fracture toughness, probably because the composite plies adapted to the bent shape of the titanium substrates.

#### 4.3.2. Analysis of the fracture surfaces and failure modes of TC joints

To further explain the trend of the R-curves for the titanium-CFRP joints, Fig. 16 shows the correspondent fracture surfaces.

It can be seen how similar failure modes characterised batches TC-O S, TC-NO AP and TC-NO S, where the failure was mainly mixed cohesive-adhesive in the first part of crack propagation, followed by crack deflection in the composite for all the samples excluding TC-O S1. For

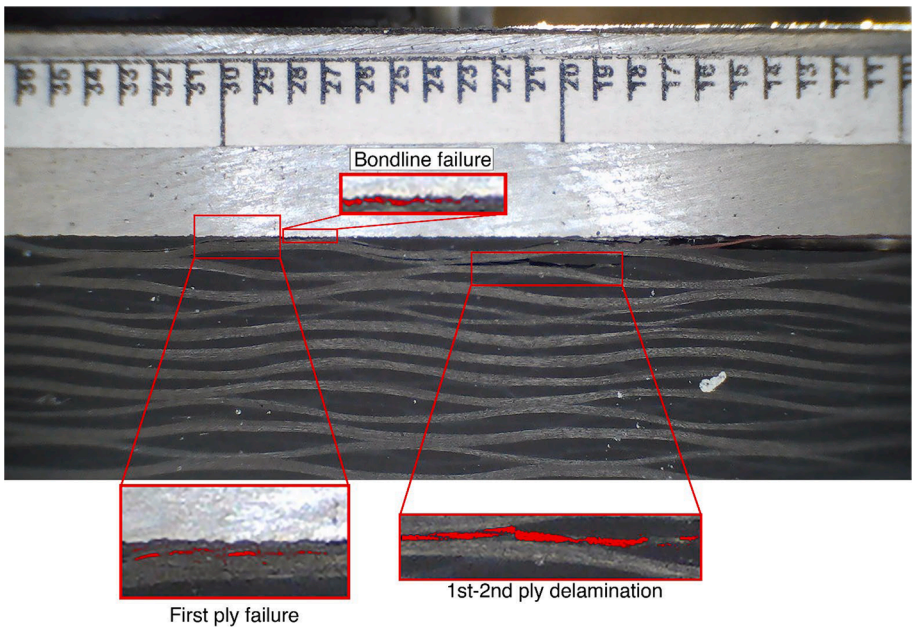


**Fig. 17.** Competition between multiple crack fronts (sample TC-NO S2): at the bondline, inside the first ply and between the first and the second ply.

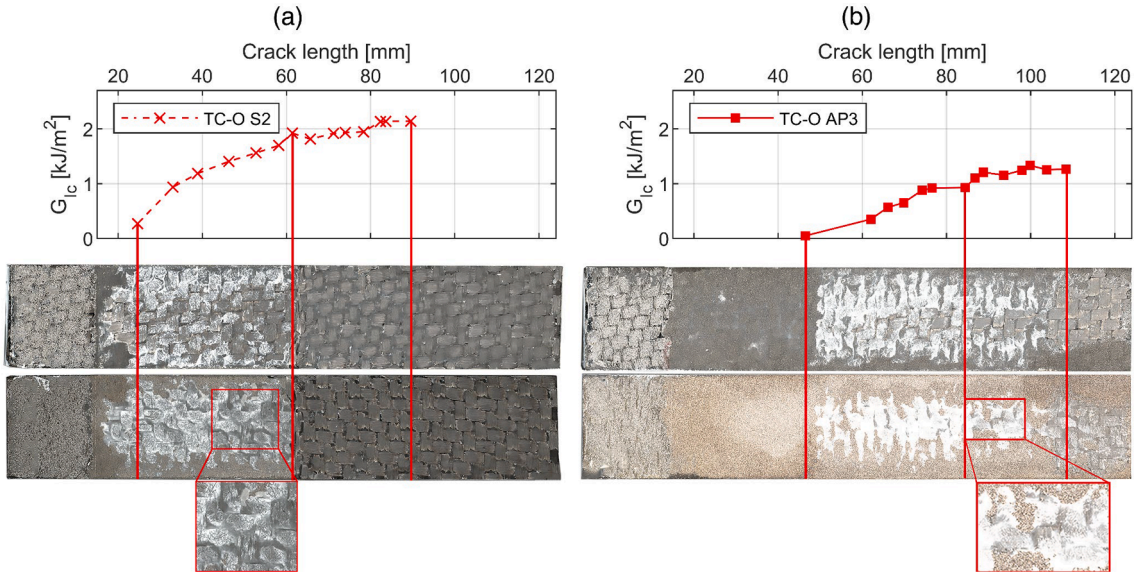


**Fig. 18.** (a) Joint TC-O S2, R-curve against fracture surface. the red lines indicate, from left to right: crack position at beginning of the test, crack deflection in the composite and crack position at the end of the test. residues of carbon fibres on the titanium adherend. b) Fracture surfaces and R-curve of the TC-O AP3 joint. Titanium adherend shown below CFRP adherend. The first part of the test is characterised by oxide layer failure, leading to brittle crack propagation starting from the first unloading. Traces of carbon fibres on the titanium substrate suggest first-ply failure.

the TC-O AP joints, which were the worst performing among all the samples (0.99 kJ/m$^2$ average $G_{Ic}$), the failure modes were mainly adhesive and oxide layer fracture, as with the metal–metal joints.

It is worth noting that residues of carbon fibres are left on the titanium adherends in all the samples, suggesting first-ply failure. The authors believe that the rising trend of fracture toughness associated with these failure modes is due to the competition between multiple crack locations (Fig. 17), namely at the bondline, in the first ply and between the composite adherend's first and second ply. Similar observations were made in the work by Lima et al. [54], where CFRP-CFRP secondary bonded DCB joints with different stacking sequences were tested to assess the influence of the CFRP layup on the fracture toughness and failure mechanisms.

#### 4.3.3. *Comparison of TC-O S and TC-O AP joints*

The significantly higher fracture toughness of the TC-O S joints compared to the TC-O AP batch (+62 % average $G_{Ic}$) is reflected on their fracture surfaces, as shown in Fig. 16 and Fig. 18.

Fig. 18 plots the R-curves and compares them with the fracture surfaces. For sample TC-O S2 (Fig. 18**a),** in the first part of the test, the failure was mixed cohesive-adhesive with the presence of carbon fibre residues increasing with the crack propagation (first ply failure) and a significant rise in fracture toughness, resulting from the multiple competing crack fronts, as discussed earlier. As the fracture toughness reached 1.92 kJ/m$^2$, the crack deflected between the first and second ply of the laminate, with the R-curve settling to a steadier trend. It is worth noting that right before the crack deflection, a peak in the fracture

toughness was recorded, followed by a decrease after the crack deflected in the composite, as was also observed by Lima et al. [54]. Specimen TC-O S3 had a similar fracture behaviour, whereas crack deflection was not recorded in joint TC-O S1, which had the lowest fracture toughness in the batch.

As shown in Fig. 18**b**, in the TC-O AP3 joint the crack propagates in the oxide layer from 15 mm to 45 mm of length. In this area, no traces of adhesive are left on the titanium adherend, whereas dark residues of oxide cover the adhesive layer in the composite substrate. This behaviour was also observed in [38], where the annealed samples treated at a temperature above 750 °C formed a brittle scale of oxide that broke during the test, leading to worse performance than the untreated coupons. From 45 mm to 85 mm, the increasing trend of fracture toughness can be associated with a mixed cohesive-adhesive failure, with cohesive failure in the central portion of the joint and adhesive failure on the sides at the adhesive-titanium interface. A further increase of toughness can be seen from 85 mm of crack propagation until the end of the test, where carbon fibre debris is left on the titanium substrate, suggesting first-ply failure. The switch to mixed cohesive-adhesive failure and eventually to crack deflection was beneficial for the toughness, which rose up to 1.26 kJ/m$^2$ in the last unloading. A similar behaviour also characterised sample TC-O AP1, whereas no first ply failure was seen in sample TC-O AP2, which had the lowest strength in the batch and a flatter R-curve (0.67 kJ/m$^2$ average and 0.61 kJ/m$^2$ initial fracture toughness).

It is worth noting that the crack position is well captured by the CBBM method as can be seen in Fig. 18, since the crack deflection positions and the changes in failure mechanisms are in good accordance with the R-curves.

The comparable values of fracture toughness of the TC-NO AP (1.46 kJ/m$^2$) and TC-NO S (1.56 kJ/m$^2$) batches were reflected by similar failure modes, with mixed cohesive-adhesive failure, first ply failure and crack deflection for all 6 joints (Fig. 16). For the non-oxidised joints, the sandblasting treatment had a significantly lower influence on the fracture toughness (+6.8 % average $G_{Ic}$). It can be concluded that the passivation oxide layer forming at ambient temperature does not hinder the adhesion strength of LPBF −printed titanium joints, hence the sandblasting treatment can be avoided.

## 5. Conclusions

This work aimed at exploring the possibility to bond LPBF Ti6Al4V parts without surface treatments and assessing the influence of thermal oxidation arising from the post-printing high temperature treatment, which is commonly carried in industrial applications of LPBF components to relieve residual stresses. Based on the results, the following conclusions can be drawn:

- Titanium surface characterisation: the as-printed surfaces have more peaks compared to the sandblasted surfaces (+60 % average skewness $S_{ssk}$ over the sandblasted specimens) likely attributable to the partially melted particles stuck on the surface. After sandblasting, the roughness is reduced on both the oxidised (−31 % $S_a$) and non-oxidised (–23 % $S_a$) samples and the wettability is significantly improved in both non-oxidised (14 % contact angle reduction) and oxidised (35 % contact angle reduction) samples. The increase in wettability is in accordance with the Cassie-Baxter model [49] for the estimation of contact angle, where an increase of surface roughness leads to a decrease in wettability. Moreover, the sandblasting promotes the removal of surface contamination. The XPS analysis shows how the annealing treatment shifts the titanium-α peaks to the left and induces the formation of aluminium oxides ($Al_2O_3$) and titanium oxides ($TiO_2$) on the surface of the samples, proving that the thermal treatment induces high-temperature oxidation on the titanium adherends.
- Metal-metal joints fracture toughness: the sandblasting did not have a positive effect on the fracture toughness of the TT-NO joints (−39 %). This behaviour was associated with the presence of residual stresses as the NO samples were not thermally treated, which released after the sandblasting, resulting in bending of the adherends prior to bonding. The bent adherends are forced into a straight configuration during the high-pressure cure cycle, preloading the adhesive before the test and thus reducing the fracture toughness of the TC-NO S batch.
- Metal-composite joints fracture toughness: the oxidation arising from the thermal stress-relieving process is detrimental for the adhesion strength the as-printed non-oxidised batch, with the non-oxidised joints having 47 % higher average fracture toughness compared to the oxidised as-printed samples. The sandblasting proves to be an effective method in removing the oxide scales and thus promoting cohesive failure instead of breakage of the brittle oxides. Sandblasting improved by 62 % the toughness of the oxidised joints, while leading to only a minor improvement of 7 % for non-oxidised joints.

In this work, it is shown that the as-printed surface of LPBF Ti6Al4V has great potential in both metal–metal and metal-composite adhesively bonded joints, given its inherently rough surface morphology that can be exploited to avoid time-consuming surface treatments. Nevertheless, the presence of oxide scales resulting from the thermal treatment hinders the adhesion strength of the as-printed surface due to the brittle failure of the oxides. Moreover, the as-printed samples showed a higher percentage of adhesive failure, which could be concerning for long-term durability due to humidity infiltration in the cracks at the adherend-adhesive interface, degrading the mechanical properties of the adhesive [55]. The results of this work thus bring to light the necessity to further investigate the optimisation of the thermal treatments of LPBF titanium in the context of adhesive bonding.

## CRediT authorship contribution statement

**Michele Gulino:** Writing – original draft, Methodology, Investigation, Formal analysis, Conceptualization. **Rosemere de Araujo Alves Lima:** Writing – review & editing, Methodology, Investigation, Formal analysis, Conceptualization. **Fabrizio Moroni:** Writing – review & editing, Supervision, Project administration, Conceptualization. **Alessandro Pirondi:** Writing – review & editing, Supervision, Project administration, Conceptualization. **Sofia Teixeira de Freitas:** Writing – review & editing, Supervision, Project administration, Conceptualization.

## Declaration of competing interest

*The authors declare that they have no known competing financial interests or personal relationships that could have appeared to influence the work reported in this paper.*

## Acknowledgements

This research was carried as part of the project DOT13SJY60, Ministerial Decree No. 1061 of 10/08/2021 and funded under the “Programma Operativo Nazionale” (PON), Action IV.4 “PhD grant on Innovation Thematics”. Significant support was provided by Bercella Srl and 3 T-Additive manufacturing that kindly provided the materials for this research. The authors would also like to thank, Peter Jerrard, Matteo Menoni, and Ulderico Tarasconi for their invaluable advice, guidance, and expertise during the experimental campaign and the development of this research. The authors acknowledge Fundação para a Ciência e a Tecnologia (FCT) for its financial support via the project LAETA Base Funding (10.54499/UIDB/50022/2020).”

## Data availability

Data will be made available on request.

## References


[1] Z. Wang, X. Jin, Q. Li, G. Sun, On crashworthiness design of hybrid metal-composite structures, Int. J. Mech. Sci. 171 (Apr. 2020), https://doi.org/10.1016/j.ijmecsci.2019.105380.

[2] R. Subbaramaiah, B.G. Prusty, G.M.K. Pearce, S.H. Lim, R.S. Thomson, Crashworthy response of fibre metal laminate top hat structures, Compos. Struct. 160 (Jan. 2017) 773–781, https://doi.org/10.1016/j.compstruct.2016.10.112.

[3] P. Spiros, Revolutionizing Aircraft Materials and Processes, Springer International Publishing, 2020, https://doi.org/10.1007/978-3-030-35346-9.

[4] G. Marsh, Airbus A350 XWB update, Reinf. Plast. 54 (6) (2010) 20–24, https://doi.org/10.1016/S0034-3617(10)70212-5.

[5] P. P. Camanho and F. L. Matthews, "Stress analysis and strength prediction of mechanically fastened joints in FRP: a review," 1997.

[6] da Silva L.F.M., Öchsner A., and Adams R.D., Handbook of Adhesion Technology. Springer Berlin Heidelberg, 2011. 10.1007/978-3-642-01169-6.

[7] D.A. Dillard, Advances in Structural Adhesive Bonding, Pergamon vol. 18, no. 1 (2011), https://doi.org/10.1016/J.ENGFAILANAL.2010.09.010.

[8] F. Moroni, F. Musiari, C. Favi, Effect of the surface morphology over the fatigue performance of metallic single lap-shear joints, Int. J. Adhes. Adhes. 97 (Mar. 2020), https://doi.org/10.1016/j.ijadhadh.2019.102484.

[9] F. Moroni, F. Musiari, A. Pirondi, Influence of laser ablation-induced surface topology on the mechanical behaviour of aluminium bonded joints, Proceedings of the Institution of Mechanical Engineers, Part l: Journal of Materials: Design and Applications 233 (3) (Mar. 2019) 505–520, https://doi.org/10.1177/1464420718813388.

[10] Y. Dai, S. Zhao, F. Qin, T. An, Y. Gong, P. Chen, Shear fracture resistance enhancement through micropatterning on copper substrate for sintered nano silver joints, Int. J. Adhes. Adhes. 125 (Jul. 2023), https://doi.org/10.1016/j.ijadhadh.2023.103422.

[11] C. Ashforth and L. Ilcewicz, "Certification of Bonded Aircraft Structure and Repairs." [Online]. Available: https://f10011.eos-intl.net/F10011/OPAC/TileStart.aspx.

[12] T. A. Schmid Fuertes, T. Kruse, T. Körwien, and M. Geistbeck, "Bonding of CFRP primary aerospace structures - Discussion of the certification boundary conditions and related technology fields addressing the needs for development," Compos Interfaces, vol. 22, no. 8, pp. 795–808, Oct. 2015, 10.1080/09276440.2015.1077048.

[13] F. Moroni, A. Pirondi, C. Pernechele, L. Vescovi, Comparison of Tensile Strength and Fracture Toughness of Co-Bonded and Cold-Bonded Carbon Fiber Laminate-Aluminum Adhesive Joints, Materials (2021), https://doi.org/10.3390/ma14143778.

[14] S.T. De Freitas, J. Sinke, Adhesion properties of bonded composite-to-aluminium joints using peel tests, J. Adhes. 90 (5–6) (Jun. 2014) 511–525, https://doi.org/10.1080/00218464.2013.850424.

[15] C. Morano, A. Wagih, M. Alfano, G. Lubineau, Improving performance of composite/metal T-joints by using corrugated aluminum stiffeners, Compos. Struct. 307 (Mar. 2023), https://doi.org/10.1016/j.compstruct.2022.116652.

[16] F. Smith, COMELDTM: An innovation in composite to metal joining, Mater. Technol. 20 (2) (2005) 91–96, https://doi.org/10.1080/10667857.2005.11753117.

[17] W. Tu, P. Wen, P. Hogg, F.J. Guild, Optimisation of the protrusion geometry in ComeldTM joints, Compos. Sci. Technol. 71 (6) (Apr. 2011) 868–876, https://doi.org/10.1016/j.compscitech.2011.02.001.

[18] W. Tu, P. Wen, and F. J. Guild, "The optimization of ComeldTMjoints: A novel technique for bonding composites and metal," in World Congress on Engineering: WCE 2010, Newswood Ltd., 2010, pp. 1383–1385.

[19] A.L. Buxton, B.G.I. Dance, Surfi-SculptTM - Revolutionary surface processing with an electron beam, in: Surface Engineering - Proceedings of the 4th International Surface Engineering Conference, 2005, pp. 107–110.

[20] W. Xiong, X. Wang, J.P. Dear, B.R.K. Blackman, The effect of protrusion density on composite-metal joints with surfi-sculpt reinforcement, Compos. Struct. 180 (Nov. 2017) 457–466, https://doi.org/10.1016/j.compstruct.2017.08.036.

[21] X. Wang, J. Ahn, Q. Bai, W. Lu, J. Lin, Effect of forming parameters on electron beam Surfi-Sculpt protrusion for Ti-6Al-4V, Mater. Des. 76 (Jul. 2015) 202–206, https://doi.org/10.1016/j.matdes.2015.03.065.

[22] S. Ucsnik, M. Scheerer, S. Zaremba, D.H. Pahr, Experimental investigation of a novel hybrid metal-composite joining technology, Compos. A Appl. Sci. Manuf. 41 (3) (Mar. 2010) 369–374, https://doi.org/10.1016/j.compositesa.2009.11.003.

[23] P.N. Parkes, R. Butler, J. Meyer, A. de Oliveira, Static strength of metal-composite joints with penetrative reinforcement, Compos. Struct. 118 (1) (2014) 250–256, https://doi.org/10.1016/j.compstruct.2014.07.019.

[24] L. Raimondi, L. Tomesani, L. Donati, A. Zucchelli, Lattice material infiltration for hybrid metal-composite joints: Manufacturing and static strenght, Compos. Struct. 269 (Aug. 2021), https://doi.org/10.1016/j.compstruct.2021.114069.

[25] A. P. Mouritz, "Review of z-pinned composite laminates," Dec. 2007. 10.1016/j.compositesa.2007.08.016.

[26] S.K. Everton, M. Hirsch, P. Stravroulakis, R.K. Leach, A.T. Clare, Review of in-situ process monitoring and in-situ metrology for metal additive manufacturing, Mater. Des. 95 (Apr. 2016) 431–445, https://doi.org/10.1016/j.matdes.2016.01.099.

[27] M. Grasso, B.M. Colosimo, Process defects and in situ monitoring methods in metal powder bed fusion: a review, Meas. Sci. Technol. 28 (4) (Apr. 2017) 044005, https://doi.org/10.1088/1361-6501/aa5c4f.

[28] M. Bugatti and B. M. Colosimo, "A new method for in-situ process monitoring of AM cooling rate-related defects," in Procedia CIRP, Elsevier B.V., 2021, pp. 325–329. 10.1016/j.procir.2021.03.101.

[29] A.M. Khorasani, I. Gibson, A.R. Ghaderi, Rheological characterization of process parameters influence on surface quality of Ti-6Al-4V parts manufactured by selective laser melting, Int. J. Adv. Manuf. Technol. 97 (9–12) (Aug. 2018) 3761–3775, https://doi.org/10.1007/s00170-018-2168-6.

[30] G. Strano, L. Hao, R.M. Everson, K.E. Evans, Surface roughness analysis, modelling and prediction in selective laser melting, J. Mater. Process. Technol. 213 (4) (2013) 589–597, https://doi.org/10.1016/j.jmatprotec.2012.11.011.

[31] W. Cai, Q. Song, H. Ji, M.K. Gupta, Multi-perspective analysis of building orientation effects on microstructure, mechanical and surface properties of slm ti6al4v with specific geometry, Materials 14 (16) (2021) Aug, https://doi.org/10.3390/ma14164392.

[32] M. Ahmed, M.A. Obeidi, S. Yin, R. Lupoi, Influence of processing parameters on density, surface morphologies and hardness of as-built Ti-5Al-5Mo-5V-3Cr alloy manufactured by selective laser melting, J. Alloy. Compd. 910 (Jul. 2022), https://doi.org/10.1016/j.jallcom.2022.164760.

[33] E. Ertürk, B. Musil, G. Diez, C. Felber, P. Höfer, Surface morphology influences of PBF-LB manufactured Ti6Al4V parts on adhesive bond strength—investigation of as-built and surface-treated conditions, Prog. Addit. Manuf. (2023), https://doi.org/10.1007/s40964-023-00450-7.

[34] C. Koch, J. Richter, M. Vollmer, M. Kahlmeyer, T. Niendorf, S. Böhm, Adhesively bonded joints in components manufactured via selective laser melting, Proc. Inst. Mech. Eng. C J. Mech. Eng. Sci. 235 (3) (Feb. 2021) 518–526, https://doi.org/10.1177/0954406220959376.

[35] L.A. Ardila-Rodríguez, C. Rans, J.A. Poulis, Effect of surface morphology on the Ti–Ti adhesive bond performance of Ti6Al4V parts fabricated by selective laser melting, Int. J. Adhes. Adhes. 110 (Oct. 2021), https://doi.org/10.1016/j.ijadhadh.2021.102918.

[36] A.T.T. Nguyen, M. Brandt, A.C. Orifici, S. Feih, Hierarchical surface features for improved bonding and fracture toughness of metal-metal and metal-composite bonded joints, Int. J. Adhes. Adhes. 66 (Apr. 2016) 81–92, https://doi.org/10.1016/j.ijadhadh.2015.12.005.

[37] Z. Fielden-Stewart, T. Coope, D. Bacheva, B.C. Kim, Effect of the surface morphology of SLM printed aluminium on the interfacial fracture toughness of metal-composite hybrid joints, Int. J. Adhes. Adhes. 105 (Mar. 2021), https://doi.org/10.1016/j.ijadhadh.2020.102779.

[38] M. Antanasova, A. Kocjan, A. Abram, J. Kovač, P. Jevnikar, Pre-oxidation of selective-laser-melted titanium dental alloy: effects on surface characteristics and porcelain bonding, J. Adhes. Sci. Technol. 35 (19) (2021) 2094–2109, https://doi.org/10.1080/01694243.2021.1877003.

[39] M. Gulino, F. Moroni, A. Pirondi, Metal-metal and metal-composite joints with 3D printed aluminium substrates: effect of surface treatment on the mode I fracture toughness, J. Adhes. (2023), https://doi.org/10.1080/00218464.2023.2285074.

[40] ASTM E8/E8M-22, "Standard Test Methods for Tension Testing of Metallic Materials." 10.1520/E0008_E0008M-13A.

[41] M. Yan and P. Yu, "An Overview of Densification, Microstructure and Mechanical Property of Additively Manufactured Ti-6Al-4V — Comparison among Selective Laser Melting, Electron Beam Melting, Laser Metal Deposition and Selective Laser Sintering, and with Conventional Powder," in Sintering Techniques of Materials, InTech, 2015, ch. 5. 10.5772/59275.

[42] W. Wang, R. Lopes Fernandes, S. Teixeira De Freitas, D. Zarouchas, and R. Benedictus, "How pure mode I can be obtained in bi-material bonded DCB joints: A longitudinal strain-based criterion," Compos B Eng, vol. 153, pp. 137–148, Nov. 2018, 10.1016/j.compositesb.2018.07.033.

[43] "HexBond TM ST1035 Epoxy Film Adhesive," 2018.

[44] "ASTM D3433 - DCB Metal Joints".

[45] M.F.S.F. de Moura, R.D.S.G. Campilho, J.P.M. Gonçalves, Crack equivalent concept applied to the fracture characterization of bonded joints under pure mode I loading, Compos. Sci. Technol. 68 (10–11) (Aug. 2008) 2224–2230, https://doi.org/10.1016/j.compscitech.2008.04.003.

[46] R.D.F. Moreira, M.F.S.F. de Moura, F.G.A. Silva, A novel strategy to obtain the fracture envelope under mixed-mode I+II loading of composite bonded joints, Eng. Fract. Mech. 232 (Jun. 2020), https://doi.org/10.1016/j.engfracmech.2020.107032.

[47] "Fibre-reinforced plastic composites - Determination of mode I interlaminar fracture toughness, GIC , for unidirectionally reinforced materials," 2001.

[48] R.N. Wenzel, Resistance of solid surfaces to wetting by water, Ind. Eng. Chem. (1936).

[49] A.B.D. Cassie, S. Baxter, Wettability of porous surfaces, Trans. Faraday Soc. 40 (1944) 546–551, https://doi.org/10.1039/tf9444000546.

[50] T. Thenard, A. Catapano, R. Allena, M. El May, N. Saintier, M. Mesnard, Topography and wettability characterization of surfaces manufactured by SLM and treated by chemical etching, Mech. Adv. Mater. Struct. 29 (12) (2022) 1674–1691, https://doi.org/10.1080/15376494.2020.1836292.

[51] S. Wang, Y. Liu, C. Zhang, Z. Liao, W. Liu, The improvement of wettability, biotribological behavior and corrosion resistance of titanium alloy pretreated by thermal oxidation, Tribol. Int. 79 (2014) 174–182, https://doi.org/10.1016/j.triboint.2014.06.008.

[52] P. Sarria, et al., "Processing and characterization of Ti-6Al-4V samples manufactured by selective laser melting," in Key Engineering Materials, Trans Tech

Publications Ltd (2016) 260–268, https://doi.org/10.4028/www.scientific.net/KEM.704.260.

[53] G.D. Lima, B.L. Nascimento, I. de Souza Alves, M.P. Júnior, Trindade, and S. Griza,, Fatigue behavior and life predictions of thermally oxidized Ti6Al4V alloy according to oxidation parameters, Eng. Fail. Anal. 130 (2021) Dec, https://doi.org/10.1016/j.engfailanal.2021.105737.

[54] R.A.A. Lima, R. Tao, A. Bernasconi, M. Carboni, N. Carrere, S. Teixeira de Freitas, Uncovering the toughening mechanisms of bonded joints through tailored CFRP layup, Compos. B Eng. 263 (Aug. 2023), https://doi.org/10.1016/j.compositesb.2023.110853.

[55] C.S.P. Borges, E.A.S. Marques, R.J.C. Carbas, C. Ueffing, P. Weißgraeber, L.F.M. D. Silva, Review on the effect of moisture and contamination on the interfacial properties of adhesive joints, Proc. Inst. Mech. Eng. C J. Mech. Eng. Sci. 235 (3) (Feb. 2021) 527–549, https://doi.org/10.1177/0954406220944208.